

# Exploring orbital dynamics and trapping with a generalized pilot-wave framework

Lucas D. Tambasco, and John W. M. Bush

Citation: *Chaos* **28**, 096115 (2018); doi: 10.1063/1.5033962

View online: <https://doi.org/10.1063/1.5033962>

View Table of Contents: <http://aip.scitation.org/toc/cha/28/9>

Published by the [American Institute of Physics](#)

---

---



**Chaos**  
An Interdisciplinary Journal of Nonlinear Science

**Fast Track Your Research. *Submit Today!***

# Exploring orbital dynamics and trapping with a generalized pilot-wave framework

Lucas D. Tambasco and John W. M. Bush<sup>a)</sup>

*Department of Mathematics, Massachusetts Institute of Technology, Cambridge, Massachusetts 02139, USA*

(Received 7 April 2018; accepted 9 July 2018; published online 24 September 2018)

We explore the effects of an imposed potential with both oscillatory and quadratic components on the dynamics of walking droplets. We first conduct an experimental investigation of droplets walking on a bath with a central circular well. The well acts as a source of Faraday waves, which may trap walking droplets on circular orbits. The observed orbits are stable and quantized, with preferred radii aligning with the extrema of the well-induced Faraday wave pattern. We use the stroboscopic model of Oza *et al.* [J. Fluid Mech. **737**, 552–570 (2013)] with an added potential to examine the interaction of the droplet with the underlying well-induced wavefield. We show that all quantized orbits are stable for low vibrational accelerations. Smaller orbits may become unstable at higher forcing accelerations and transition to chaos through a path reminiscent of the Ruelle-Takens-Newhouse scenario. We proceed by considering a generalized pilot-wave system in which the relative magnitudes of the pilot-wave force and drop inertia may be tuned. When the drop inertia is dominated by the pilot-wave force, all circular orbits may become unstable, with the drop chaotically switching between them. In this chaotic regime, the statistically stationary probability distribution of the drop's position reflects the relative instability of the unstable circular orbits. We compute the mean wavefield from a chaotic trajectory and confirm its predicted relationship with the particle's probability density function. *Published by AIP Publishing.* <https://doi.org/10.1063/1.5033962>

**A pilot-wave system consists of a particle guided by its own wavefield. Walking droplets are the first macroscopic realization of a pilot-wave system, displaying features once thought to be peculiar to quantum mechanics, including quantized orbits. Here, we explore how quantized orbits may arise when the droplet interacts with a background wavefield. We show experimentally that a well at the center of a vibrating fluid bath excites a circularly-symmetric Faraday wavefield, which may serve to trap a walking drop. The stable quantized radii correspond to the extrema of the Faraday wavefield induced by the well. We proceed to explore this trapping theoretically, using the stroboscopic model of Oza *et al.*<sup>1</sup> Modeling the underlying wave as an external potential, we characterize the stability of the resulting quantized orbits and characterize the transition to chaos for unstable orbits. We then consider a generalized pilot-wave system in which the relative magnitudes of the drop inertia and pilot-wave force may be tuned, allowing us to explore parameter regimes characterized by the stable orbits observed experimentally, as well as unstable orbits between which walkers switch chaotically. In this chaotic regime, we explore the relationship between the drop's statistics and its mean wavefield.**

## I. INTRODUCTION

The vertical and horizontal dynamics of a droplet walking on a vibrating fluid bath have been a subject of considerable recent interest.<sup>2,3</sup> The walking droplet system is the

first macroscopic realization of a pilot-wave system of the form envisioned by Louis de Broglie,<sup>4</sup> displaying various quantum-like features, including quantized orbits,<sup>5,6</sup> double quantization,<sup>7,8</sup> tunneling,<sup>9,10</sup> and the emergence of multimodal statistics in confined geometries.<sup>11,12</sup> In this hydrodynamic pilot-wave system, walking droplets generate a wave at impact with the bath surface and are, in turn, piloted by the resulting superposition of waves. The temporal decay time of the waves  $T_M$  increases monotonically with vibrational acceleration  $\gamma$ , provided  $\gamma$  is less than  $\gamma_F$ , the Faraday threshold above which waves form on the surface in the absence of a drop. The horizontal motion of the droplet depends on the gradient of the pilot wave at the impact position, and a time-averaged drag term proportional to the droplet's velocity.<sup>1,13</sup> A drop's trajectory may be further affected by an external force acting on the drop, such as a Coriolis force, which arises on a rotating bath,<sup>5,6,14,15</sup> or a linear spring force as generated from a magnetic field acting on a drop with encapsulated ferrofluid.<sup>7,8,16,17</sup> These scenarios may be modeled by incorporating an additional force term into the stroboscopic trajectory equation of Oza *et al.*<sup>1</sup>

The majority of walker studies have been undertaken in the deep-water limit, in which the walker wavefield decays in amplitude nearly to zero before reaching the lower boundary of the bath, so the walker dynamics is uninfluenced by bottom topography. In their study of walker motion in elliptical corrals, Sáenz *et al.* demonstrated the viability of pilot-wave hydrodynamics in shallow water.<sup>12</sup> Furthermore, they demonstrated that, in this shallow-water regime, bottom topography can be used to serve as effective potentials. Specifically, they demonstrated that submerged circular wells act to attract walkers and so play

<sup>a)</sup>Electronic mail: bush@math.mit.edu

a role analogous to magnetic impurities in the quantum corrals.<sup>18</sup> Motivated by their insights, we here examine the interaction of a walker with a submerged circular well in an otherwise open system.

We are motivated by an experiment in which a walking droplet interacts with the wavefield produced by a circular well at the center of the bath. In the deep region, the vibrational acceleration  $\gamma$  exceeds the Faraday threshold  $\gamma_F$ . Outside the well,  $\gamma < \gamma_F$ ; thus, the well excites a circularly symmetric Faraday wave across the bath that decays beyond the well. Tambasco *et al.*<sup>19</sup> showed that an unstable checkerboard Faraday wave pattern may trap walking droplets, causing them to bounce in place. We investigate here how the well-induced circularly-symmetric Faraday pattern may trap the droplet onto circular orbits.

The stability of circular orbits in a rotating frame<sup>14</sup> and in a harmonic potential<sup>8,16</sup> have been characterized theoretically using the stroboscopic model of Oza *et al.*<sup>1</sup> In both settings, an increase in forcing acceleration destabilized circular orbits into wobbling and eventually chaotic orbits.<sup>20</sup> Tambasco *et al.*<sup>21</sup> characterized the transition to chaos for both these external forces, as well as for a 2-dimensional Coulomb force. Walking drops acted upon by a Coriolis or Coulomb force underwent a period-doubling cascade, while drops in a harmonic potential became chaotic via a path reminiscent of the Ruelle-Takens-Newhouse scenario.<sup>22,23</sup> Here, we characterize the transition to chaos for a particle in a circular orbit over a well-induced wavefield. We model the well-induced wave as an oscillatory force field with characteristic wavelength  $\lambda_F$  and a spatial decay rate corresponding to that of a Bessel function.

When the vibrational forcing acceleration is sufficiently high, a droplet will explore the domain of a uniform bath erratically. Provided the memory time is larger than the crossing time of the bath, coherent statistics will emerge in the

drop's position probability density function.<sup>11,12</sup> Durey *et al.*<sup>24</sup> derived that the mean wavefield  $\bar{\eta}$  is related to the droplet's stationary probability distribution  $\mu(x)$  via a convolution with the bouncer wavefield  $\eta_B$  (Theorem 1). Here, we validate this relationship between mean wavefield and position distribution in the case of a particle interacting with a well-induced wavefield. We further characterize numerically the timescale of convergence to this asymptotic result.

In Sec. II, we describe the experimental methods and present trajectories of a droplet walking on a bath with a well-induced wavefield. In Sec. III, we present the integro-differential equation used to simulate drop trajectories and discuss the numerical methods used. In Sec. IV, we present a generalized pilot-wave framework in which tuning the relative magnitudes of the inertia and wave force terms renders all circular orbits unstable. We investigate the manner in which small circular orbits destabilize for sufficiently high vibrational acceleration and characterize their transition to chaos. We also examine the relationship between the drop's mean wavefield and its statistics. We discuss the implications of these results and future directions in Sec. V.

## II. EXPERIMENTS

The experimental setup is shown in Fig. 1(a). Silicone oil with viscosity  $\nu = 20$  cS, surface tension  $\sigma = 20.9 \times 10^{-3}$  N/m, and density  $\rho = 949$  kg/m<sup>3</sup> fills a circular container with a central well of radius  $d = 12$  mm. The fluid depth is  $h_1 = 6.5 \pm 0.1$  mm inside the well and  $h_0 = 5.5 \pm 0.1$  mm outside. The bath is vibrated vertically with frequency  $f = 80$  Hz, amplitude  $A$ , and acceleration  $\Gamma(t) = \gamma \cos(2\pi ft)$ , where  $\gamma = A(2\pi f)^2$ . When the vibrational acceleration of the bath  $\gamma$  exceeds a critical value, the Faraday threshold  $\gamma_F$ , the surface of the bath becomes unstable, and subharmonic waves (with Faraday period  $T_F = 2/f$ ) appear throughout the bath.<sup>25</sup>

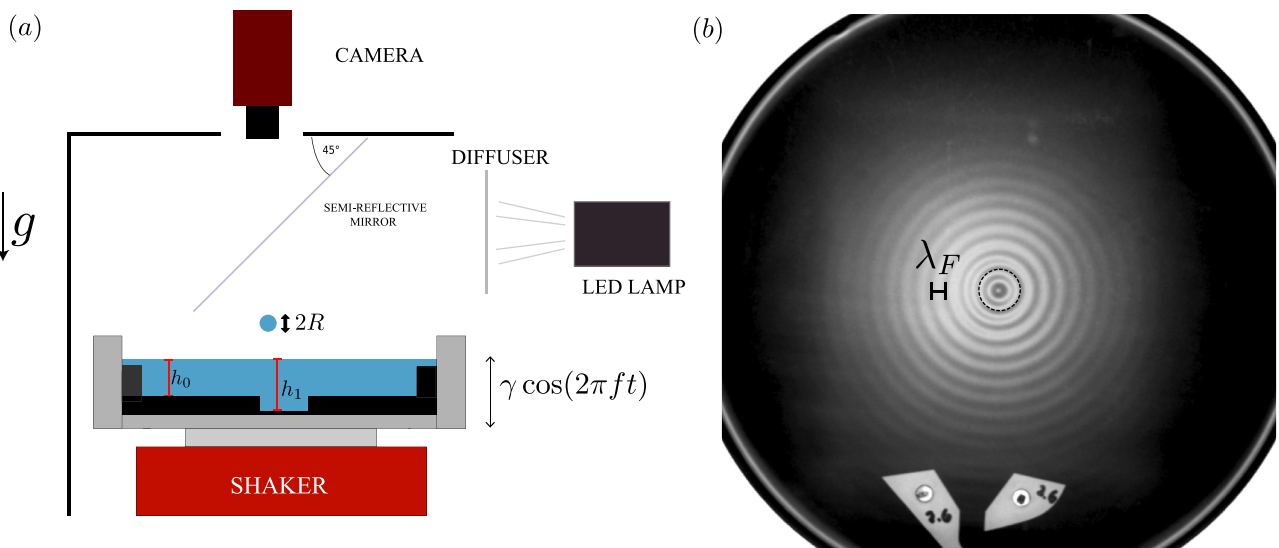


FIG. 1. (a) Experimental setup. A droplet of radius  $R$  bounces on a bath vibrating vertically with frequency  $f = 80$  Hz and vibrational acceleration  $\gamma$ , with a central circular well of depth  $h_1 = 6.5$  mm. The depth elsewhere is  $h_0 = 5.5$  mm. The experiment is imaged from above, illuminated by diffused light via a semi-reflective mirror. (b) Top view of the most unstable circularly-symmetric Faraday mode induced by the well for  $\gamma = 4.0g$ . The boundary of the well is delineated by a dashed line. The Faraday threshold has been crossed only in the region directly above the well so that  $\gamma_F^d < \gamma < \gamma_F^s$ , where  $\gamma_F^d$  and  $\gamma_F^s$  are the Faraday thresholds in the deep and shallow regions, respectively.

We note that the Faraday threshold decreases with depth of the fluid bath. Denoting the Faraday thresholds in the deep and shallow regions by  $\gamma_F^d$  and  $\gamma_F^s$ , we operate in a regime such that  $\gamma_F^d < \gamma < \gamma_F^s$ . Consequently, the deep fluid serves as a source of Faraday waves that decay beyond the well [Fig. 1(b)].

The wave number of the most unstable Faraday mode,  $k_F$ , is obtained from the standard water-wave dispersion relation,

$$\omega_F^2(k) = \left( gk + \frac{\sigma}{\rho} k^3 \right) \tanh(kh), \quad (1)$$

where  $\omega_F = \pi f$  is the subharmonic angular frequency and  $g$  the gravitational acceleration. Between the shallow ( $h_0 = 5.5$  mm) and deep ( $h_1 = 6.5$  mm) regions, the Faraday wavelength changes negligibly, taking the values of  $\lambda_F = 2\pi/k_F = 4.75 \pm .01$  mm, within measurement errors.

A drop of radius  $R = 0.4 \pm 0.01$  mm deposited onto the surface of a vibrating fluid bath bounces indefinitely, provided the vibrational acceleration of the bath  $\gamma$  is sufficiently large. At each impact, the drop generates a circularly symmetric wave centered at its bouncing position. Provided that  $\gamma < \gamma_F$ , the amplitude of such waves decay in time, with a characteristic time-scale  $T_M = T_d/(1 - \gamma/\gamma_F)$ , where  $T_d \sim \lambda_F^2/\nu \approx 0.018$  s is the decay time of waves in the absence of vibration. As the vibrational acceleration is increased further, the bouncing state destabilizes and the drop begins to walk in response to the gradient of the underlying wavefield. A drop walking below the Faraday threshold performs rectilinear motion in the absence of boundaries and external forces at a free speed prescribed by the balance of the propulsive wave force and a linear drag.<sup>1,13</sup>

In the presence of the well, the walker interacts with a well-induced wavefield. To characterize this interaction, we track the position of droplets walking on the corrugated wavefield (Fig. 2). For all initial conditions considered, droplets lock onto stable circular orbits. Droplets initially placed in unstable positions wobble until eventually settling onto a stable orbit. Circular orbits are separated by half the Faraday wavelength  $\lambda_F/2$ . This spacing may be understood by considering the possibility of the drop bouncing in- or out-of-phase, relative to the both vibration, and that a  $\pi$ -shift in its bouncing phase will reverse the stability of its circular orbits. We proceed by investigating the drop's interaction with the well-induced wavefield using the stroboscopic model of Oza *et al.* with an additional topographically-induced potential.<sup>1,12</sup>

### III. TRAJECTORY EQUATION

Building upon the model of Moláček & Bush,<sup>13</sup> Oza *et al.* developed an integro-differential trajectory equation to describe the horizontal motion of a droplet of mass  $m$  walking on a vibrating fluid bath.<sup>1</sup> The droplet's trajectory,  $\mathbf{x}_p(t) = [x_p(t), y_p(t)]$ , is given by

$$m\ddot{\mathbf{x}}_p + D\dot{\mathbf{x}}_p = -mg\nabla h|_{\mathbf{x}=\mathbf{x}_p(t)} + \mathcal{F}(|\mathbf{x}_p(t)|), \quad (2)$$

where  $D$  is the time-averaged drag coefficient,  $g$  the gravitational acceleration, and  $\mathcal{F}(|\mathbf{x}_p(t)|)$  an externally applied radial force to be specified. Provided the vertical bouncing timescale  $T_F$  is much smaller than the horizontal time scale  $\lambda_F/|\dot{\mathbf{x}}|$ ,

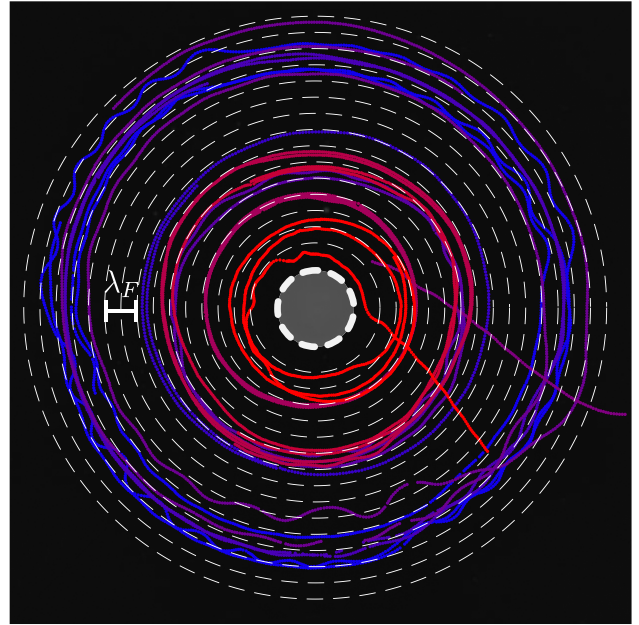


FIG. 2. Preliminary experimental trajectories of droplets of radius  $R = 0.4 \pm 0.01$  mm walking in the Faraday wavefield shown in Fig. 1(b), with forcing acceleration  $\gamma = 4.0$  g. The droplets tend to stabilize onto quantized circular orbits, with preferred radii corresponding roughly to half-integer multiples of the Faraday wavelength  $\lambda_F$ . Each color corresponds to a different trajectory, with white dashed lines indicating orbits of half-integer multiples of the Faraday wavelength,  $r = n/2\lambda_F$ .

or equivalently, the drop's vertical speed greatly exceeds its horizontal speed, the wavefield  $h$  may be approximated as an integral

$$h(\mathbf{x}, t) = \frac{\bar{A}}{T_F} \int_{-\infty}^t J_0(k_F |\mathbf{x} - \mathbf{x}_p(s)|) e^{-(t-s)/T_M} ds, \quad (3)$$

where  $\bar{A}$  is the wave amplitude.

If we take the natural length and time scales to be the Faraday wavelength  $\lambda_F$  and the memory time  $T_M$ , we may non-dimensionalize Eq. (2) via  $\tilde{\mathbf{x}} = k_F \mathbf{x}$ ,  $\tilde{t} = t/T_M$ . Dropping tildes, we obtain the dimensionless equation:

$$\kappa \ddot{\mathbf{x}}_p + \dot{\mathbf{x}}_p = \beta \int_{-\infty}^t \frac{J_1(|\mathbf{x}_p(t) - \mathbf{x}_p(s)|)}{|\mathbf{x}_p(t) - \mathbf{x}_p(s)|} \times [\mathbf{x}_p(t) - \mathbf{x}_p(s)] e^{-(t-s)} ds + \tilde{\mathcal{F}}(|\mathbf{x}_p(t)|), \quad (4)$$

where

$$\kappa = m/DT_M, \quad \beta = Fk_F T_M^2/DT_F \quad (5)$$

are, respectively, the non-dimensional drop inertia and pilot-wave force parameters, with  $F = mgAk_F$ .  $\tilde{\mathcal{F}}(\tilde{\mathbf{x}}_p) = k_F T_M \mathcal{F}(\mathbf{x}_p)/D$  is the externally applied force. We note that this corresponds to the Generalized Pilot-wave Framework (GPF) outlined by Bush,<sup>3</sup> as will be further explored in Sec. IV.

We proceed by specifying the imposed external force  $\mathcal{F}(|\mathbf{x}_p(t)|)$  whose form is chosen in order to best match the influence of the well-induced wavefield. We model the well-induced standing Faraday wave as a subharmonic, circularly-symmetric Bessel function of the first kind, with wavelength  $\lambda_F$ :  $h_w(\mathbf{x}, t) = A_w J_0(|k_F \mathbf{x}|) \sin(\pi f t)$ , where  $A_w$  is the well-induced wave amplitude. A walking drop in the (2,1)

mode<sup>13</sup> resonant with the well-induced wave will feel a normal force prescribed by the gradient of the standing wave,  $\mathcal{F}(\mathbf{x}_p) = -mg \nabla h_w|_{\mathbf{x}=\mathbf{x}_p(t)}$ . In non-dimensional terms, we thus obtain

$$\tilde{\mathcal{F}}(\mathbf{x}_p) = QJ_1(|x_p(t)|)\hat{\mathbf{r}}, \quad (6)$$

where  $Q = mgA_w k_F^2 T_M \sin(\phi)/D$  is the dimensionless well-induced wave force parameter,  $\hat{\mathbf{r}}$  the unit radial vector, and  $\sin(\phi)$  the vertical phase, selected to match the experimental free walking speed.<sup>1</sup> We solve the integro-differential system [Eq. (4)] using a fourth-order Adams-Bashforth linear multistep method.<sup>15</sup>

Circular orbits of radius  $r_0$  and orbital angular speed  $\omega$ ,  $\mathbf{x}_p(t) = r_0[\cos(\omega t), \sin(\omega t)]$ , are solutions to Eq. (4) provided they satisfy the following system of algebraic equations:

$$\begin{aligned} -\kappa r_0 \omega^2 &= \beta \int_0^\infty J_1\left(2r_0 \sin\left(\frac{\omega z}{2}\right)\right) \sin\left(\frac{\omega z}{2}\right) e^{-z} dz + QJ_1(r_0), \\ r_0 \omega &= \beta \int_0^\infty J_1\left(2r_0 \sin\left(\frac{\omega z}{2}\right)\right) \cos\left(\frac{\omega z}{2}\right) e^{-z} dz. \end{aligned} \quad (7)$$

We solve Eq. (7) in order to obtain the values of  $\omega$  and  $Q$  corresponding to various initial radii  $r_0$ . We initialize the simulations assuming circular orbits of radius  $r_0$  for time  $t < 0$ . At  $t = 0$ , we impose an external force given by Eq. (6) and solve the system using a non-dimensional time-step  $\Delta t/T_M = 2^{-8}$ . Figure 3 displays trajectories simulated for  $\gamma/\gamma_F = 0.9$ , superimposed on the wavefield observed experimentally. We see that the radii of stable, quantized orbits deduced numerically correspond roughly to the extrema of the well-induced Faraday wavefield, indicating that the external force proposed in Eq. (6) is sufficient to capture the behavior observed experimentally. We note that trajectories initialized at unstable radii wobble until eventually tending to a stable circular orbit, as in experiments. For the forcing accelerations ( $0.85 < \gamma/\gamma_F < 0.99$ ) and initial radii ( $0.1 < r_0/\lambda_F < 3$ ) considered, trajectories always settled into stable orbital solutions, corresponding approximately to the zeros of  $J_1(r)$ , where the imposed force field vanishes. We note that the prevalence of circular orbits at radii corresponding to the zeros of  $J_0(r)$  has been noted in a number of prior studies of orbital pilot-wave dynamics.<sup>6,7,14,16,20,26</sup> In our study, the imposed potential evidently shifts the preferred orbits to zeros of  $J_1(r)$ .

#### IV. GENERALIZED PILOT-WAVE FRAMEWORK

One can imagine much richer system behavior, including chaotic switching between unstable orbits, as has been observed in a number of hydrodynamic quantum analogs.<sup>6,8,11,12,20,26</sup> In order to characterize such chaotic switching states, we consider a combination of oscillatory and harmonic potentials. Furthermore, with a view to characterizing transitions to unstable regimes, we proceed by exploring a generalized pilot-wave framework, where the externally applied force and system parameters  $\beta$  and  $\kappa$  may be altered relative to those of the fluid system. Particular attention will be given to characterizing how circular orbits destabilize and quantum-like statistics emerge.

In order to destabilize the circular orbits observed in simulations of droplets walking in an oscillatory potential

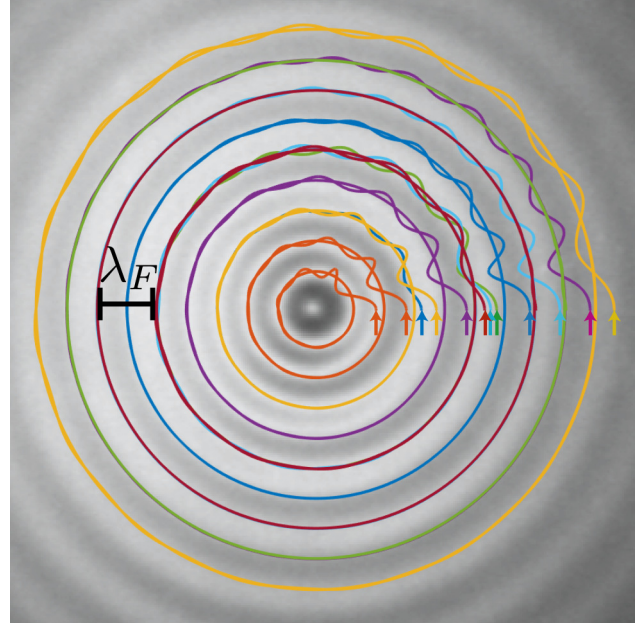


FIG. 3. Droplet trajectories calculated from the stroboscopic model [Eq. (2)] with an additional oscillatory force prescribed by Eq. (6), superimposed on the experimental wavefield from Fig. 1(b). Trajectories were initialized in circular orbits with various initial radii, indicated by colored arrows. After small oscillations, all trajectories converged onto stable quantized orbits separated by half-integer multiples of the Faraday wavelength  $\lambda_F$ .

(Fig. 3), we introduce an additional force term into the stroboscopic model [Eq. (4)]. Specifically, to the Bessel force [Eq. (6)] we add a radial force arising from a harmonic potential,  $\mathcal{F}(\mathbf{x}_p) = -k\mathbf{x}_p$ , where  $k$  is the non-dimensional spring constant. As we vary the relative magnitudes of the spring and wave force parameters,  $k$  and  $Q$ , circular orbits may become unstable. For a fixed value of the spring constant  $k = 0.1$ , we note that lowering  $Q$  prompts a transition from stable to wobbling, and eventually, chaotic orbits, as detailed in Fig. 4.

#### A. Transition to Chaos

We here detail the manner in which smaller circular trajectories ( $r/\lambda_F \sim 0.5$ ) transition to chaos in this generalized pilot-wave system with both oscillatory and harmonic potentials. We consider a fixed spring constant  $k = 0.1$  and well-induced wave force coefficient  $Q = 0.3$ . We vary non-dimensional parameters  $\beta$  and  $\kappa$  according to the vibrational forcing acceleration  $\gamma/\gamma_F$  in a manner prescribed by Eq. (5). We increase the forcing acceleration gradually and analyze the stability of the resulting orbits. The transition to chaos for smaller orbits is summarized in Fig. 4, where columns correspond, respectively, to the particle's trajectory, the radius as a function of time, and frequency decomposition of the radius signal.

We initialize the drop in a stable circular orbit of radius  $r/\lambda_F = 0.5$  and  $\gamma/\gamma_F = 0.94$  and introduce a small non-dimensional perturbation  $\delta x/\lambda_F = 0.01$  at  $t = 0$ . We track the drop radius as a function of time; for stable circular orbits, the initial perturbation decays exponentially and the drop radius tends to a constant. As  $\gamma/\gamma_F$  is increased gradually, the circular orbit destabilizes. For  $\gamma/\gamma_F > 0.945$ , the initial perturbation grows exponentially until eventually settling

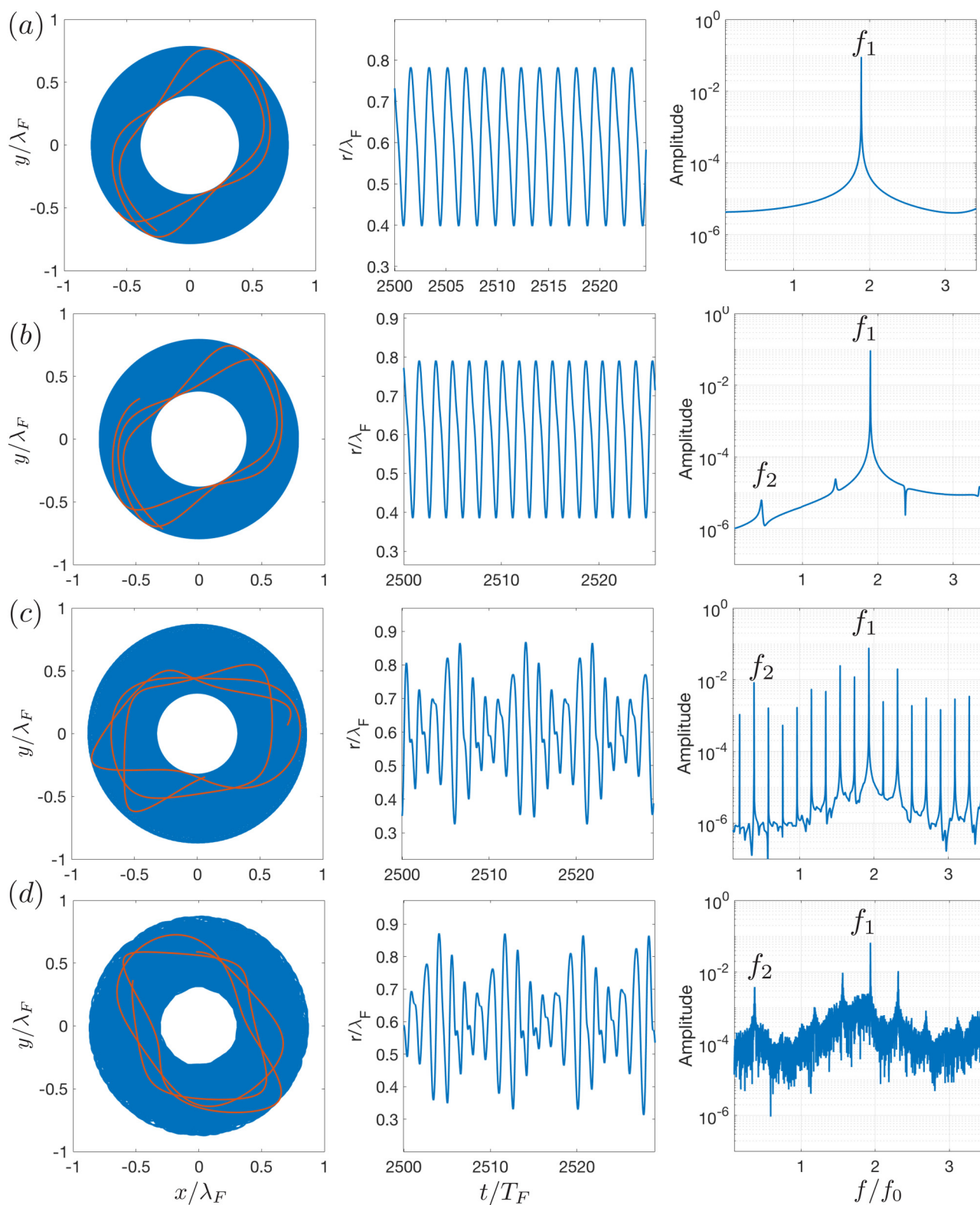


FIG. 4. The first column corresponds to the simulated trajectories of walking droplets in a generalized pilot-wave framework with  $Q = 0.3$ ,  $k = 0.1$ . A few orbital periods are highlighted in red. The second column shows the radius of the drop as a function of time, with corresponding frequency spectrum presented in the third column. (a) The onset of wobbling at  $\gamma/\gamma_F = 0.945$ , where the wobbling frequency is approximately twice the orbital frequency,  $f_1 \approx 2f_0$ . Since the emergent frequency is slightly less than twice the orbital frequency, the periodic trajectory precesses. (b) A second, incommensurate frequency  $f_2$  appears at  $\gamma/\gamma_F \sim 0.963$ , corresponding to small-amplitude modulations in wobbling. (c)  $\gamma/\gamma_F = 0.9667$ . (d) The wobbling state destabilizes when  $\gamma/\gamma_F > 0.9668$ , being replaced by a chaotic trajectory characterized by a broadband frequency spectrum. We note that the transition to chaos occurs over a narrow range of  $\Delta\gamma/\gamma_F$ , requiring high numerical precision beyond that attainable experimentally.

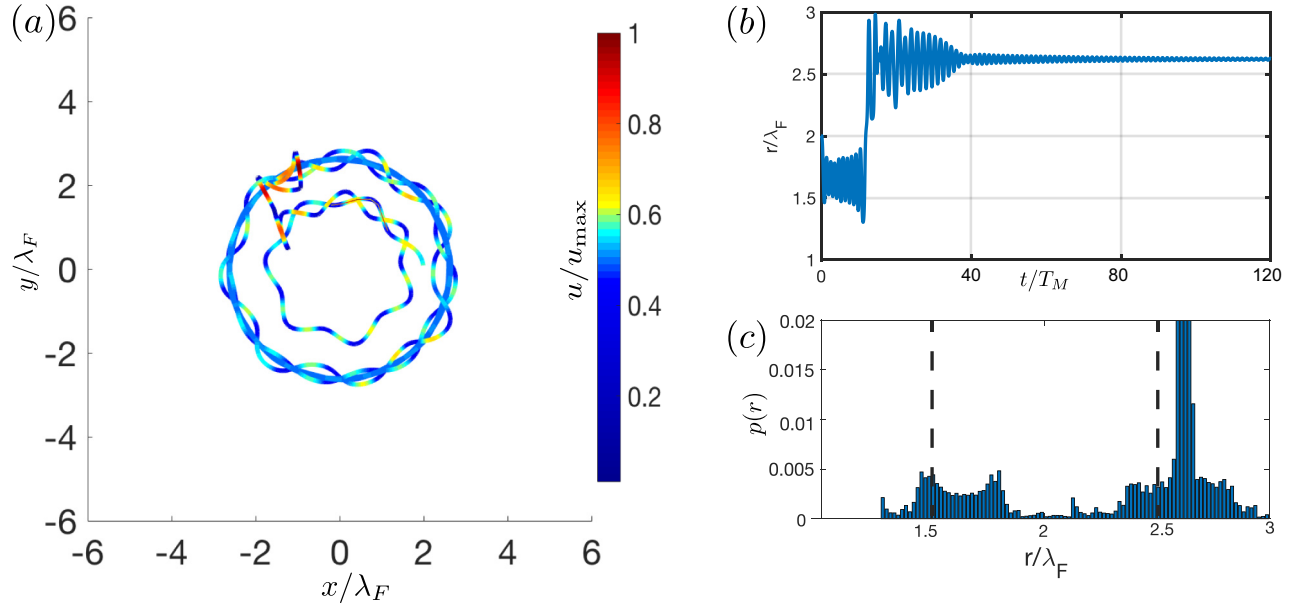


FIG. 5. An orbit initialized at an unstable radial position ( $r_0/\lambda_F \sim 1.5$ ) wobbles until settling onto a larger stable radius. The most stable orbits correspond closely to the zeros of the Bessel function  $J_1(x)$ . (a) Trajectory of a single drop with  $\kappa = 0.14$ ,  $\beta = 252.8$ , simulated from Eq. (4) with  $\gamma/\gamma_F = 0.97$ ,  $Q = 0.3$ , and  $k = 0.1$ , with time step  $\Delta t/T_M = 2^{-8}$  and total time  $t_{\max}/T_M = 120$ . The trajectory is color-coded according to drop speed. (b) The corresponding radius as a function of time and (c) the probability distribution,  $p(r)$ . The transient state is short-lived, with the drop locking onto the next largest orbital state ( $r/\lambda_F \sim 2.5$ ).

onto a non-linear wobbling state [Fig. 4(a)]. The orbital radius wobbles periodically between two values, with a wobbling frequency  $f_1 \approx 2f_0$ , where  $f_0$  is the orbital frequency. When  $\gamma/\gamma_F \sim 0.963$  [Fig. 4(b)], a second, incommensurate frequency  $f_2$  emerges in the power spectrum, with  $f_2/f_1 \approx 0.24$ . The lower frequency corresponds to the slow modulation in the radius signal. The amplitude of the modulation increases with  $\gamma/\gamma_F$ , reaching its maximal value at  $\gamma/\gamma_F = 0.9667$  [Fig. 4(c)]. Finally, for  $\gamma/\gamma_F > 0.9668$ , the orbit

becomes chaotic, as suggested by the broadband frequency spectrum shown in Fig. 4(d).

## B. Emerging statistics

We may further explore the generalized pilot-wave framework by altering the dependence of the pilot-wave force  $\beta$  and the inertial coefficient  $\kappa$  parameters relative to those arising in the fluid system ( $\kappa \in (0, 1.5)$ ,

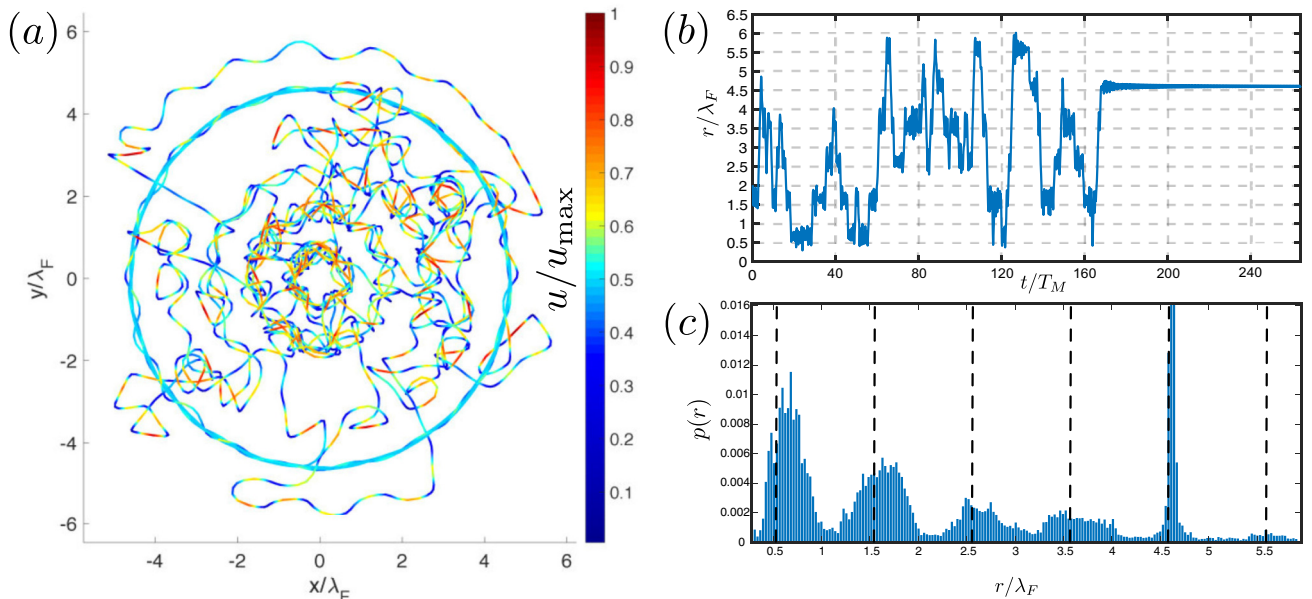


FIG. 6. Transient approach to a stable orbit deduced numerically from the generalized pilot-wave framework. (a) A single drop with  $\kappa = 0.14$ ,  $\beta = 252.8$ , simulated from Eq. (4) with  $\gamma/\gamma_F = 0.98$ ,  $Q = 0.3$ , and  $k = 0.1$ , with time step  $\Delta t/T_M = 2^{-8}$  and total time  $t_{\max}/T_M = 250$ . The trajectory is color-coded according to drop speed. (b) Corresponding radius as a function of time and (c) probability distribution. During its long transient, the drop explores 6 orbitals before locking onto the second largest ( $r/\lambda_F \sim 4.5$ ).

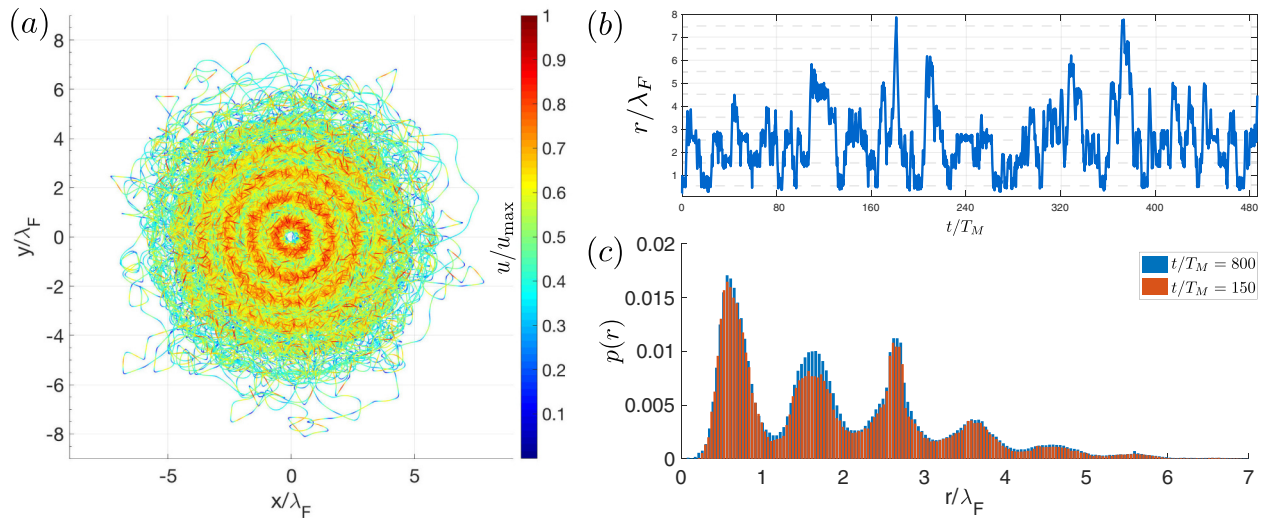


FIG. 7. (a) Trajectory of a walker switching chaotically between unstable orbits, as obtained from simulations of our generalized pilot-wave framework. The non-dimensional inertia  $\tilde{\kappa} = 0.042$  and pilot-wave force  $\beta = 152.8$  were tuned to render all circular orbits unstable for  $Q = 0.3$ . The trajectory is color-coded according to drop speed. (b) Radial position of the droplet as a function of time displays no periodicity. (c) The probability distribution  $p(r)$  of the drop, calculated as the number of times it was found at radius  $r$ , normalized by  $2\pi r$  and the total number of time steps. This probability distribution indicates the relative instability of the unstable circular orbits. We note that  $p(r)$  saturates after approximately  $t/T_M \sim 200$ ; thereafter, there is no significant change in the wave-like structure of the statistics.

$\beta \in [2, 500]$  for  $\gamma/\gamma_F < 0.985$ ). In particular, we seek a parameter regime characterized by unstable orbits between which walkers switch chaotically. We focus on a pilot-wave system in the large- $\beta$ , low- $\kappa$  regime, where the non-dimensional wave force is significantly larger than the non-dimensional inertial term. Physically, this corresponds to a particle with lower mass than the droplets generating a relatively high-amplitude wave. Although not realizable in a hydrodynamic setting, this regime is known to exhibit additional quantum features. For example, Oza *et al.*<sup>27</sup> show that hydrodynamic spin states characterized by a drop spontaneously orbiting in its own wavefield<sup>14,28</sup> are stable in this regime.

At low forcing acceleration  $\gamma/\gamma_F = 0.95$ , corresponding to  $\beta = 40.5$ ,  $\kappa = 0.35$  via Eq. (5), all orbits are stable, like those shown in Fig. 3. As the forcing acceleration is increased, circular orbits tend to become unstable. We note that smaller orbits destabilize more rapidly, as seen in Fig. 5. In this case,

an orbit is perturbed from an initial radius  $r_0/\lambda_F \sim 1.5$  at  $\gamma/\gamma_F = 0.97$  and the drop begins to wobble, with an amplitude that increases until the drop reaches the next-largest stable radius,  $r/\lambda_F \sim 2.5$ . The growth of the wobbling amplitude and eventual stabilization at the next orbital radius are evident in the time series of  $r(t)$  reported in Fig. 5(b). We note that wave-like statistics begin to emerge in the drop's radial position probability density function [Fig. 5(c)]; however, a steady state is never reached, due to the eventual convergence to the stable outer orbit.

In Fig. 6(a), we see a trajectory simulated at  $\gamma/\gamma_F = 0.98$  ( $\beta = 252.8$ ,  $\kappa = 0.14$ ) where a structure of concentric rings appears in the drop's trajectory, indicating the preferred orbital radii. We track the drop's radial position as a function of time [Fig. 6(b)], which indicates that this radius does not change monotonically; rather, the drop jumps from small to large orbits and back again. The droplet eventually settles into a stable circular orbit of radius  $r/\lambda_F \approx 4.5$ ,

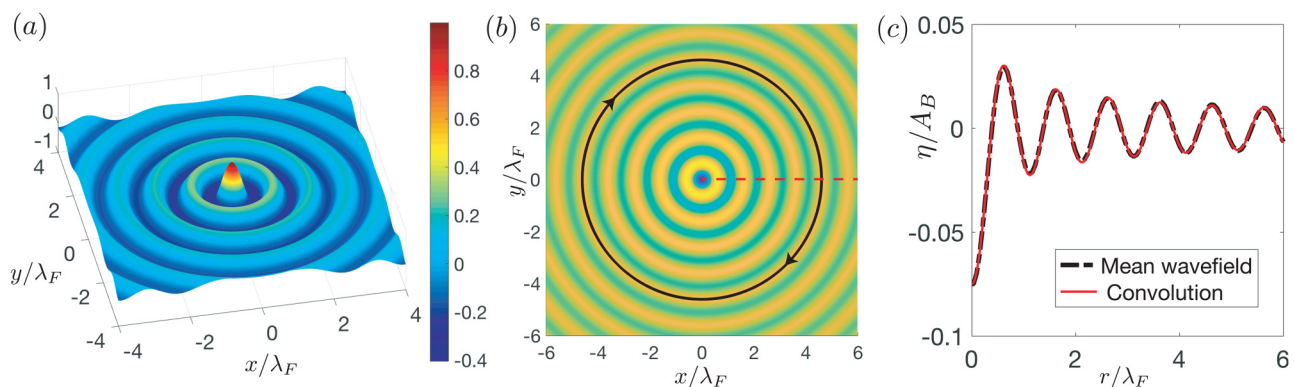


FIG. 8. (a) Non-dimensionalized wavefield of a bouncer at the origin,  $\eta_B(x)/A_B$ , computed from Eq. (3) with  $x_p(t) = 0$ . (b) A stable circular trajectory with radius  $r/\lambda_F \sim 4.5$  obtained following the transient state shown in Fig. 6(a) is superimposed onto the convolution of a bouncer wavefield and the steady pdf, given by a radial  $\delta$ -function. (c) A radial section comparing the mean wavefield computed numerically to the convolution result [Eq. (9)], for a stable circular trajectory after a time  $t/T_M \sim 50$ .

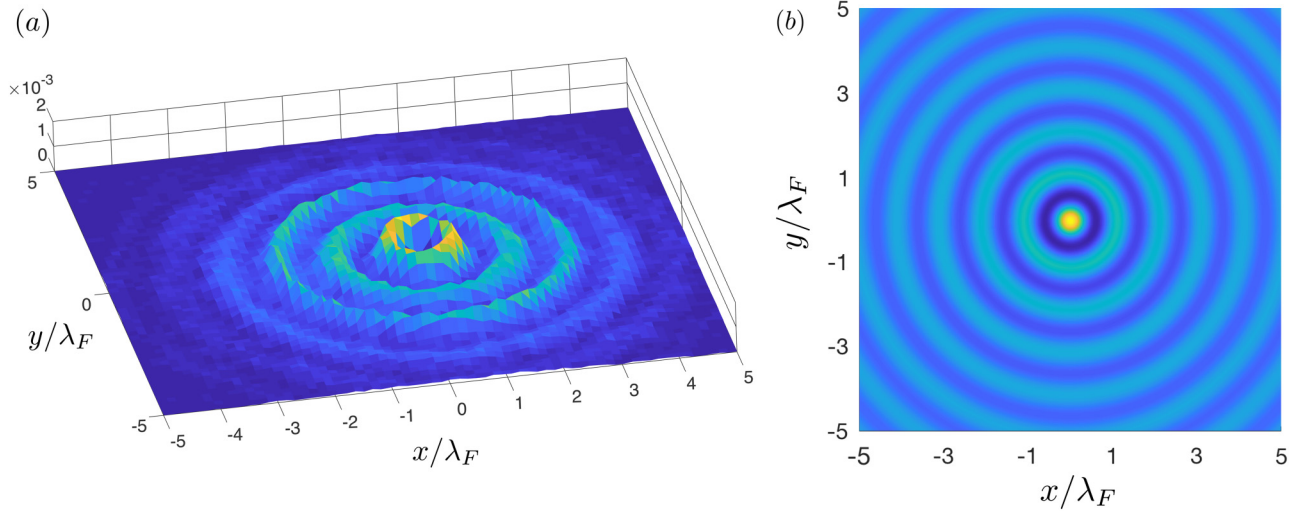


FIG. 9. The statistics and mean wavefield of the trajectory shown in Fig. 7(a). (a) Probability density function for droplet position,  $\mu(\mathbf{x})$ , generated from simulations of the generalized pilot-wave system [Eq. (4)] with non-dimensional drop inertia  $\kappa = 0.042$ , pilot-wave force  $\beta = 152.8$  and wave-force parameter  $Q = 0.3$ . The peaks of the wave-like statistics correspond to extrema of the well-induced potential. In this parameter regime, all circular orbits are unstable and the drop switches chaotically between them. (b) The convolution of bouncer wavefield and the drop's p.d.f.,<sup>24</sup>  $\eta_B(\mathbf{x}) * \mu(\mathbf{x})$  after  $t/T_M = 800$  is computed from Eq. (8). It is indistinguishable from the mean wavefield computed numerically.

after approximately  $t/T_M \sim 170$ . The preferred radial positions during the transient motion are evident in the drop's radial probability density function shown in Fig. 6(c). The preferred radii are half-integer multiples of the Faraday wavelength  $(n + 1/2)\lambda_F$ , which correspond to those of stable orbits at lower forcing accelerations.

We then lower the inertial non-dimensional coefficient  $\tilde{\kappa} = 0.7\kappa$ , while maintaining the pilot-wave force  $\beta$  as that obtained from fluid parameters with  $\gamma/\gamma_F = 0.98$ . Specifically,  $\tilde{\kappa} = 0.042$  and  $\beta = 252.8$ . The simulated trajectories are shown in Fig. 7(a). Once again, the concentric-ring structure in the particle trajectory highlights the preferred orbital radii. In this case, however, all orbits are unstable, and the droplet switches chaotically between them. We record the orbital radius as a function of time [Fig. 7(b)] and the corresponding radial probability distribution [Fig. 7(c)]. In this chaotic regime, wave-like statistics emerge in the probability density function. The probability density function (p.d.f.) saturates after approximately  $t/T_M \sim 200$  indicating the timescale of approach to a statistically steady state. Thereafter, the p.d.f. reflects the relative instability of the unstable circular orbits.

### C. Mean pilot-wave field

Durey *et al.*<sup>24</sup> demonstrated that, for unbounded systems such as this, the mean wavefield,  $\bar{\eta}(\mathbf{x}) = \lim_{t \rightarrow \infty} \int_0^t h(\mathbf{x}, \tau) d\tau/t$ , is related to the emerging statistics through the convolution:

$$\bar{\eta}(\mathbf{x}) = \int_{\mathcal{R}^2} \eta_B(\mathbf{x} - \mathbf{y})\mu(\mathbf{y}) d\mathbf{y}, \quad (8)$$

where  $\eta_B(\mathbf{x})$  is the wavefield of a bouncer at the origin [Fig. 8(a)] and  $\mu(\mathbf{x})$  is the steady probability density function for the drop's position. We proceed by verifying this relationship numerically for both periodic and chaotic orbits in our generalized pilot-wave framework.

We first consider the steady-state circular orbit that emerges following the transient behavior depicted in Fig. 6(a). In the case of a stable periodic circular orbit of radius  $r_0 \sim 4.5\lambda_F$  [Fig. 8(b)], the radial probability distribution is given by  $\mu(\mathbf{x}) = \delta(|\mathbf{x}| - r_0)/2\pi r_0$ . Since both the steady probability distribution and bouncer wavefield are radially symmetric, we may perform the required convolution [Eq. (8)] analytically in polar coordinates:

$$\frac{\bar{\eta}(r)}{A_B} = \int_{\mathcal{R}^2} \frac{J_0[\sqrt{r^2 + \rho^2 - 2r\rho \cos(\theta)}]\delta(\rho - r_0)}{2\pi r_0} \rho d\rho d\theta,$$

where  $A_B$  is the wave amplitude of a stationary bouncer. Using the identity<sup>29</sup>

$$J_0[\sqrt{r^2 + \rho^2 - 2r\rho \cos(\theta)}] = \sum_{m=0}^{\infty} \epsilon_m J_m(r) J_m(\rho) \cos(m\theta),$$

with  $\epsilon_0 = 1, \epsilon_m = 2$  for  $m \neq 0$  yields the simple result

$$\bar{\eta}(r) = A_B J_0(r) J_0(r_0). \quad (9)$$

The mean wavefield has the form of  $J_0(r)$  and an amplitude prescribed by the orbital radius  $r_0$ . The resulting convolution field along with the generating circular path are shown in Fig. 8(b). In Fig. 8(c), we compare the analytical convolution result with the mean wavefield computed numerically. The two are indistinguishable. We note that the prevalence of circular orbits on the zeros of  $J_0(r)$  reported in previous studies of orbital pilot-wave systems,<sup>6,7,14,16,20</sup> in conjunction with Eq. (9), suggests that such systems may be acting to minimize their mean wavefield and so the system energy.

For the chaotically-switching trajectory shown in Fig. 7(a), we consider a time greater than the statistical relaxation time  $t > \tau_S \sim 200T_M$  so that  $\mu(\mathbf{x})$  has converged to a statistically steady state. The steady probability distribution,  $\mu(\mathbf{x})$  [Fig. 9(a)], is then convolved with the wavefield of a bouncer,  $\eta_B(\mathbf{x})$ , resulting in the mean wavefield  $\bar{\eta}(\mathbf{x})$ .

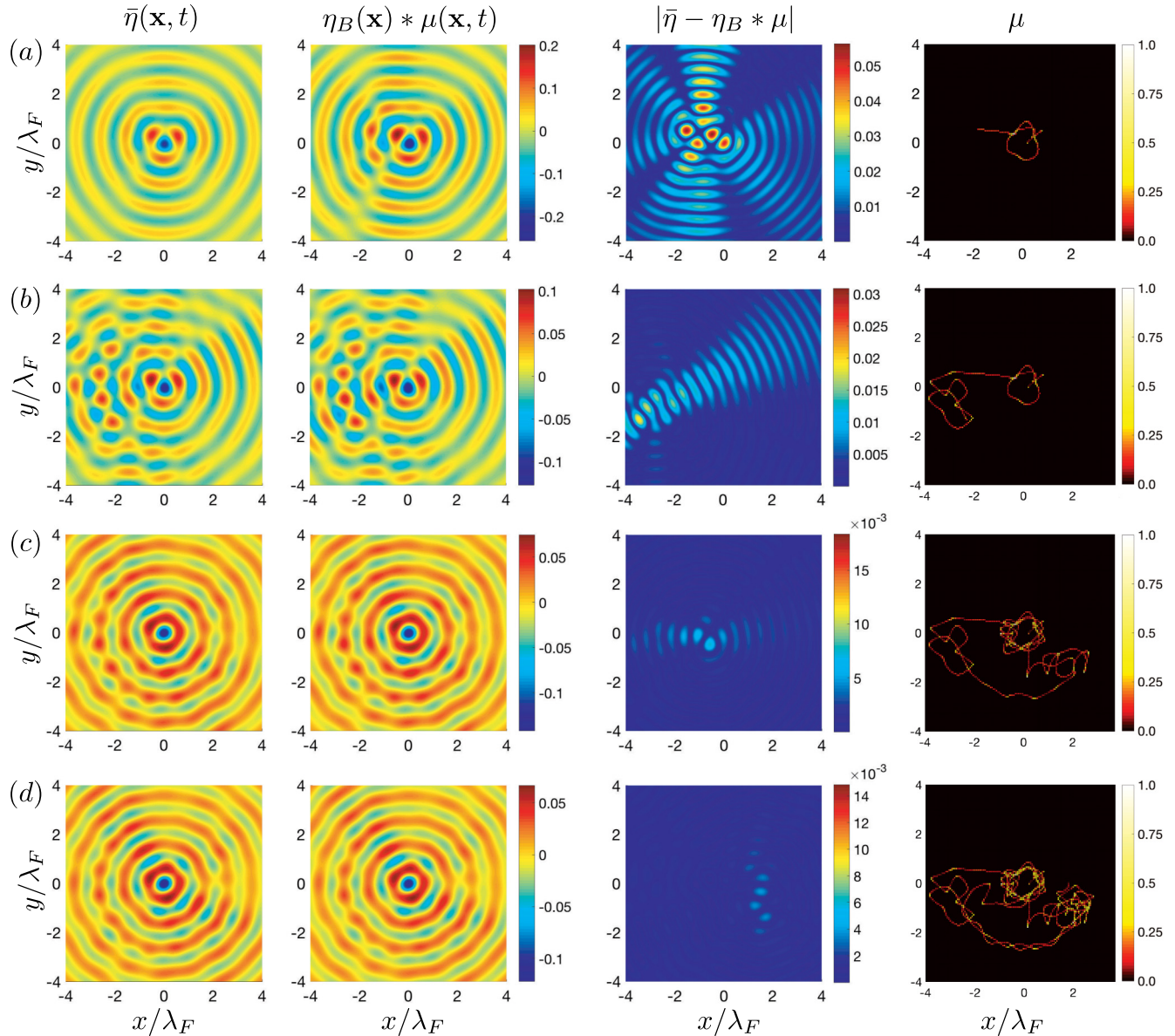


FIG. 10. First column: mean wavefield  $\bar{\eta}(x, t)$  for the chaotically-switching trajectory (Fig. 7). Second column: convolution of probability density function  $\mu(x, t)$  with stationary wavefield of a bouncer  $\eta_B(x)$ . Third column: absolute error  $|\bar{\eta}(x, t) - \mu(x, t) * \eta_B(x)|$ . Fourth column: the trajectory and associated probability density function of the drop  $\mu(x, t)$ . Bright spots correspond to peaks in  $\mu(x, t)$ , as arise at trajectory crossings and points of slow drop motion. Color bars denote relative probabilities. We track the evolution of these quantities as a function of time for (a)  $t/T_M = 3.5$ , (b)  $t/T_M = 8.2$ , (c)  $t/T_M = 22.3$ , and (d)  $t/T_M = 34.0$ .

The wavefield computed numerically and the convolution of the bouncer wavefield [Fig. 8(a)] with the probability density [Fig. 9(a)], shown in Fig. 9(b), are in accord: the root-mean square deviation computed point-wise between the two fields is  $\text{RMSD} = 2.2 \times 10^{-4}$  and decreases monotonically in time.

We now consider the evolution towards the statistical steady state. Specifically, we calculate the wavefield for the chaotically-switching trajectory via Eq. (3) and compute the resulting average wavefield numerically:

$$\bar{\eta}(x, t) = \frac{1}{t} \int_0^t h(x, \tau) d\tau. \quad (10)$$

The average wavefield in Eq. (10) converges to that from Eq. (8) over a time-scale  $\tau_S/T_M \sim 200$ , the timescale of

statistical relaxation. In Fig. 10(a), we show the computed mean wavefield  $\bar{\eta}(x, t)$ , the convolution between the bouncer wavefield with the particle's probability density function, the absolute error between the two quantities, and the particle's probability density function  $\mu(x, t)$  at time  $t/T_M = 3.5$ . At early times, there are discrepancies between the two fields, since the mean wavefield is dominated by the most recent impacts, and the particle has not explored a significant portion of the domain. At  $t/T_M = 8.2$  [Fig. 10(b)], the two quantities are qualitatively similar, with minor wave-like traces evident in the absolute error in the vicinity of the walker. As the drop explores a larger portion of the domain, as seen at later times  $t/T_M = 22.3$  [Fig. 10(c)] and  $t/T_M = 34.0$  [Fig. 10(d)], the two fields  $\bar{\eta}$  and  $\eta_B * \mu$  are effectively identical, with the error between them tending to zero globally.

## V. DISCUSSION

We have explored the horizontal dynamics of walking droplets subject to an attractive oscillatory potential. Experiments of a droplet walking on the surface of a bath with a topographically-induced Faraday wavefield demonstrate the existence of stable quantized orbits with intra-orbital spacing  $\lambda_F/2$ . The radial quantization was also observed in simulations using an integro-differential trajectory equation with an imposed oscillatory potential applied to model the influence of the underlying wavefield. Similar orbital stability characteristics were observed numerically in the parameter regime explored experimentally.

We then considered a generalized pilot-wave system where the magnitudes of the drop's inertia  $\kappa$  and pilot-wave force  $\beta$  may be tuned independently and altered relative to those appropriate for the fluid system. We also added an applied harmonic potential in order to obtain unstable circular orbits and the resulting transition to chaos. Circular orbits were shown to destabilize into wobbling, precessing, and finally, chaotic orbits. The transition from stable circular orbits to chaos is reminiscent of the Ruelle-Takens-Newhouse scenario.<sup>22,23,30</sup> In this generalized framework, there are regions in parameter space  $(\kappa, \beta)$  where all circular orbits become unstable. In this regime, drops switch chaotically between them, as has been observed in numerous orbital pilot-wave systems<sup>6,11,15,16,20</sup> The corresponding probability density for the drop's radial position shows the emergence of wave-like statistics that assume a stationary form after a time-scale  $\tau_S/T_M \sim 200$ .

We also confirmed numerically the result of Durey *et al.*<sup>24</sup> that the drop's mean wavefield is related to the emergent statistics via a convolution of the drop histogram with the wavefield of a stationary bouncer for both periodic and chaotic trajectories. We note that the existence of a unique stationary statistical distribution is not guaranteed. However, in the system considered herein, we demonstrated that such a statistically steady state emerges over the statistical relaxation time-scale  $\tau_s \sim 200T_M$ .

## ACKNOWLEDGMENTS

This work was supported by the U.S. National Science Foundation through Grant Nos. DMS-1614043 and CMMI-1727565. The authors thank Pedro J. Sáenz and Giuseppe Pucci for their assistance with the experiments and Sam Turton for the valuable discussions.

<sup>1</sup>A. U. Oza, R. R. Rosales, and J. W. M. Bush, "A trajectory equation for walking droplets: Hydrodynamic pilot-wave theory," *J. Fluid Mech.* **737**, 552–570 (2013).

<sup>2</sup>Y. Couder, S. Protière, E. Fort, and A. Boudaoud, "Dynamical phenomena: Walking and orbiting droplets," *Nature* **437**, 208 (2005).

<sup>3</sup>J. W. M. Bush, "Pilot-wave hydrodynamics," *Annu. Rev. Fluid Mech.* **47**, 269–292 (2015).

<sup>4</sup>L. de Broglie, "Interpretation of quantum mechanics by the double solution theory," *Annales de la Fondation Louis de Broglie* **12**, 1–33 (1987).

<sup>5</sup>E. Fort, A. Eddi, A. Boudaoud, J. Moukhtar, and Y. Couder, "Path-memory induced quantization of classical orbits," *Proc. Natl. Acad. Sci.* **107**, 17515–17520 (2010).

<sup>6</sup>D. M. Harris and J. W. M. Bush, "Droplets walking in a rotating frame: From quantized orbits to multimodal statistics," *J. Fluid Mech.* **739**, 444–464 (2014).

<sup>7</sup>S. Perrard, M. Labousse, M. Miskin, E. Fort, and Y. Couder, "Self-organization into quantized eigenstates of a classical wave-driven particle," *Nat. Commun.* **5**, 3219 (2014).

<sup>8</sup>M. Durey and P. A. Milewski, "Faraday wave–droplet dynamics: Discrete-time analysis," *J. Fluid Mech.* **821**, 296–329 (2017).

<sup>9</sup>A. Eddi, E. Fort, F. Moisy, and Y. Couder, "Unpredictable tunneling of a classical wave-particle association," *Phys. Rev. Lett.* **102**, 240401 (2009).

<sup>10</sup>A. Nachbin, P. A. Milewski, and J. W. M. Bush, "Tunneling with a hydrodynamic pilot-wave model," *Phys. Rev. Fluids* **2**, 034801 (2017).

<sup>11</sup>D. M. Harris, J. Moukhtar, E. Fort, Y. Couder, and J. W. M. Bush, "Wave-like statistics from pilot-wave dynamics in a circular corral," *Phys. Rev. E* **88**, 011001 (2013).

<sup>12</sup>P. J. Sáenz, T. Cristea-Platon, and J. W. M. Bush, "Statistical projection effects in a hydrodynamic pilot-wave system," *Nat. Phys.* **14**, 315–319 (2017).

<sup>13</sup>J. Moláček and J. W. M. Bush, "Drops walking on a vibrating bath: Towards a hydrodynamic pilot-wave theory," *J. Fluid Mech.* **727**, 612–647 (2013).

<sup>14</sup>A. U. Oza, D. M. Harris, R. R. Rosales, and J. W. M. Bush, "Pilot-wave dynamics in a rotating frame: On the emergence of orbital quantization," *J. Fluid Mech.* **744**, 404–429 (2014).

<sup>15</sup>A. U. Oza, Ø. Wind-Willassen, D. M. Harris, R. R. Rosales, and J. W. M. Bush, "Pilot-wave hydrodynamics in a rotating frame: Exotic orbits," *Phys. Fluids* **26**, 154101 (2014).

<sup>16</sup>M. Labousse, A. U. Oza, S. Perrard, and J. W. M. Bush, "Pilot-wave dynamics in a harmonic potential: Quantization and stability of circular orbits," *Phys. Rev. E* **93**, 033122 (2016).

<sup>17</sup>K. M. Kurianski, A. U. Oza, and J. W. M. Bush, "Simulations of pilot-wave dynamics in a simple harmonic potential," *Phys. Rev. Fluids* **2**, 113602 (2017).

<sup>18</sup>H. C. Manoharan, C. P. Lutz, and D. M. Eigler, "Quantum mirages formed by coherent projection of electronic structure," *Nature* **403**, 512–515 (2000).

<sup>19</sup>L. D. Tambasco, J. J. Pilgram, and J. W. M. Bush, "Bouncing droplet dynamics above the Faraday threshold" **28**, 096107 (2018).

<sup>20</sup>S. Perrard, M. Labousse, E. Fort, and Y. Couder, "Chaos driven by interfering memory," *Phys. Rev. Lett.* **113**, 104101 (2014).

<sup>21</sup>L. D. Tambasco, D. M. Harris, A. U. Oza, R. R. Rosales, and J. W. M. Bush, "The onset of chaos in orbital pilot-wave dynamics," *Chaos* **26**, 103107 (2016).

<sup>22</sup>D. Ruelle and F. Takens, "On the nature of turbulence," *Commun. Math. Phys.* **20**, 167–192 (1971).

<sup>23</sup>S. Newhouse, D. Ruelle, and F. Takens, "Occurrence of strange axiom A attractors near quasi periodic flows on  $T^m$ ,  $m \geq 3$ ," *Commun. Math. Phys.* **64**, 35–40 (1978).

<sup>24</sup>M. Durey, P. A. Milewski, and J. W. M. Bush, "Mean wave field effects and emerging statistics of faraday pilot-waves" (to be published).

<sup>25</sup>T. B. Benjamin and F. Ursell, "The stability of the plane free surface of a liquid in vertical periodic motion," *Proc. R. Soc. A* **225**, 505–515 (1954).

<sup>26</sup>T. Gilet, "Quantumlike statistics of deterministic wave-particle interactions in a circular cavity," *Phys. Rev. E* **93**, 042202 (2016).

<sup>27</sup>A. U. Oza, R. R. Rosales, and J. W. M. Bush, "Hydrodynamic spin states" **28**, 096106 (2018).

<sup>28</sup>M. Labousse, S. Perrard, Y. Couder, and E. Fort, "Self-attraction into spinning eigenstates of a mobile wave source by its emission back-reaction," *Phys. Rev. E* **94**, 042224 (2016).

<sup>29</sup>G. N. Watson, *A Treatise on the Theory of Bessel Functions (Cambridge Mathematical Library)* (Cambridge University Press, 1922).

<sup>30</sup>J.-P. Eckmann, "Roads to turbulence in dissipative dynamical systems," *Rev. Mod. Phys.* **53**, 643 (1981).